Supporting Information

Preparation of nitrogen-doped TiO_2-Ti_3C_2 MXene composites and its application in photocatalytic reduction of CO_2

Yilin Deng,[a] Yuqing Sun,[a] Yanxia Xu,[a,*] Jinjing Li,[a] Jiaxin Song,[a] Jiwei Qiu,[a] Juying Lei,[a,b,c,d,*]

[a] *National Engineering Research Center of Industrial Wastewater Detoxication and Resource Recovery, State Environmental Protection Key Laboratory of Environmental Risk Assessment and Control on Chemical Process, East China University of Science and Technology, 130 Meilong Road, Shanghai 200237, P. R. China. Email: xyx@ecust.edu.cn, leijuying@ecust.edu.cn*

[b] *Shanghai Institute of Pollution Control and Ecological Security, Shanghai 200092, P.R. China*

[c] *Shanghai Engineering Research Center for Multi-media Environmental Catalysis and Resource Utilization, East China University of Science and Technology, 130 Meilong Road, Shanghai 200237, P. R. China.*

2.1 Chemicals

Titanium aluminum carbide (Ti_3AlC_2, 99%) was purchased from Jilin Province Yiyi Technology Co., LTD. Lithium fluoride (LiF, 99%) was purchased from Shanghai Aladdin Biochemical Technology Co., LTD. Hydrochloric acid (HCl, 99.8%) was purchased from Sinopharm Group Chemical Reagent Co., LTD. Urea (CH_4N_2O, 99.8%) was purchased from Beijing Inokai Technology Co., LTD. High-purity carbon dioxide gas was purchased from the Air Liquide Group's Fulian plant. Deionized (DI) water was used in all experiments. All chemicals were purchased from commercial corporation with no further purification.

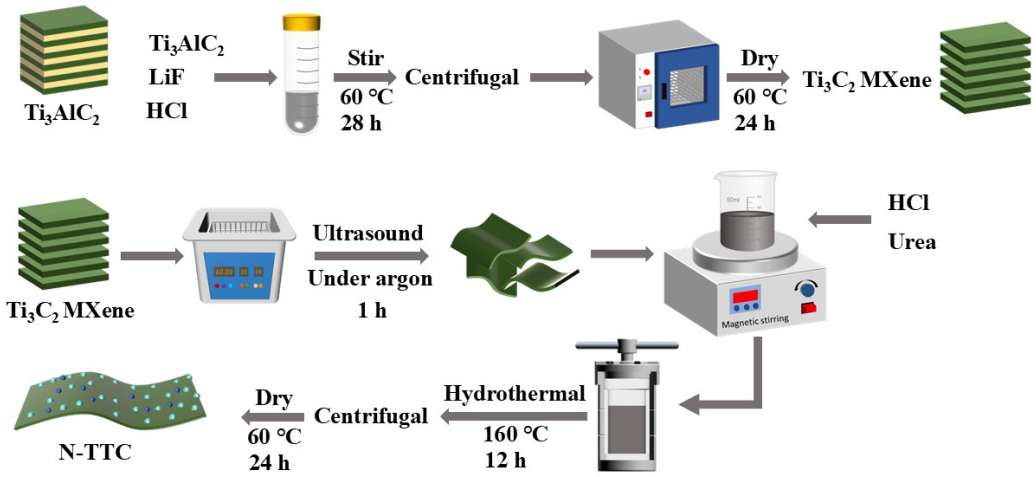

Fig. S1 Schematic illustration of the fabrication process of the N-doped Ti_3C_2 MXene-TiO_2 composite

2.2 Characterizations

2.2.1 The instrumental characterizations

The crystal structure of the catalyst was obtained using an X-ray diffraction (XRD) instrument (Rigaku D/MAX 2550 diffractometer) with Cu-Kα radiation, under conditions of 40 kV operating voltage and 100 mA operating current. The morphological characteristics of the samples were studied using scanning electron microscopy (SEM, S-4800) and transmission electron microscopy (TEM, JEM-1400). Additionally, elemental distribution analysis was conducted using the STEM mode of the Talos F200X field emission transmission electron microscope (200 kV) combined with four SuperX energy spectrum detectors. XPS data were collected using an Al Kα radiation source, with a pass energy of 150 eV and a step size of 1 eV. The valence band position of the catalyst was measured through valence band XPS (VB-XPS), allowing for quantitative determination of the valence band edge energy value of the catalytic material, and deriving its band gap width and conduction band position information in conjunction with semiconductor characteristic parameters. The ultraviolet-visible diffuse reflectance spectroscopy (UV-vis DRS) was measured

using a Shimadzu UV-3600i Plus spectrometer with an integrating sphere accessory to determine the light absorption capability of the catalyst and calculate its band gap width. Information on chemical structure and molecular interactions was obtained using surface-enhanced Raman spectroscopy (SERS). The specific surface area and pore size distribution were measured by nitrogen adsorption/desorption at 77 K using the Brunauer-Emmett-Teller (BET) model and Barrett-Joyner-Halenda (BJH) method (ASAP 2020). The isoelectric point of the photocatalyst was obtained using a zeta potential analyzer (Malvern, ZS90). The photoelectrochemical performance of the catalyst was tested on a Zahner Zennium electrochemical workstation using a standard three-electrode system: a platinum sheet as the counter electrode, a saturated calomel electrode (Hg/HgCl2) as the reference electrode, and the working electrode prepared by coating a sample film on a conductive substrate. The fluorescence properties of the samples were studied by fluorescence spectrophotometer (PL, Hitachi, F-4500). When the samples were irradiated by the excitation light source, the molecules in the samples were excited, causing them to transition to the excited state and then return to the ground state to emit fluorescence.

2.2.2 Apparent quantum efficiency (AQE) calculation

The apparent quantum yield (AQY) measurement for CO_2 photoreduction to CO was carried out under irradiation by monochromatic light (λ=400 nm). The incident light intensity was measured to be 300 mW cm^{-2} using a PL-MW2000 photoradiometer (Beijing Perfectlight Technology Co, LTD.) The effective irradiation area of the catalyst-coated glass fiber membrane was measured to be 19.63 cm^2. The electron consumption rate can be calculated from the CH_4 generation rate during the first hour of irradiation, which was 17.1 $umol \cdot g^{-1} \cdot h^{-1}$. Therefore, the AQY can be estimated according to the following formula:

$$AQY(\%) = \frac{electron\ consumption\ rate}{incident\ photon\ rate} \times 100\%$$

$$= \frac{8 \times CH_4 generating\ rate}{incident\ photo\ rate} \times 100\%$$

$$= \frac{8 \times N_A \times n(CH_4)}{P \times A \times t \times \lambda / h \times c} \times 100\%$$

$$= \frac{8 \times 6.02 \times 10^{23} \times 17.1 \times 10^{-6}}{300 \times 10^{-3} \times 19.63 \times 3600 \times 400 \times 10^{-9} / 6.626 \times 10^{-34} \times 3 \times 10^{8}} \times 100\%$$

$$= 0.05\%$$

where N_A is Avogadro's constant, n (CH_4) denotes the molar amount of CH_4, and P, A ,t, λ represent the light power density ($W \cdot cm^{-2}$), effective irradiation area (cm^2), reaction time (s), and incident light wavelength (nm), respectively. h and C denote the Planck constant and the speed of light.

Fig. S2 Labsolar-6a All-glass automatic on-line trace gas analysis system form Beijing Perfect light Technology Co., Ltd

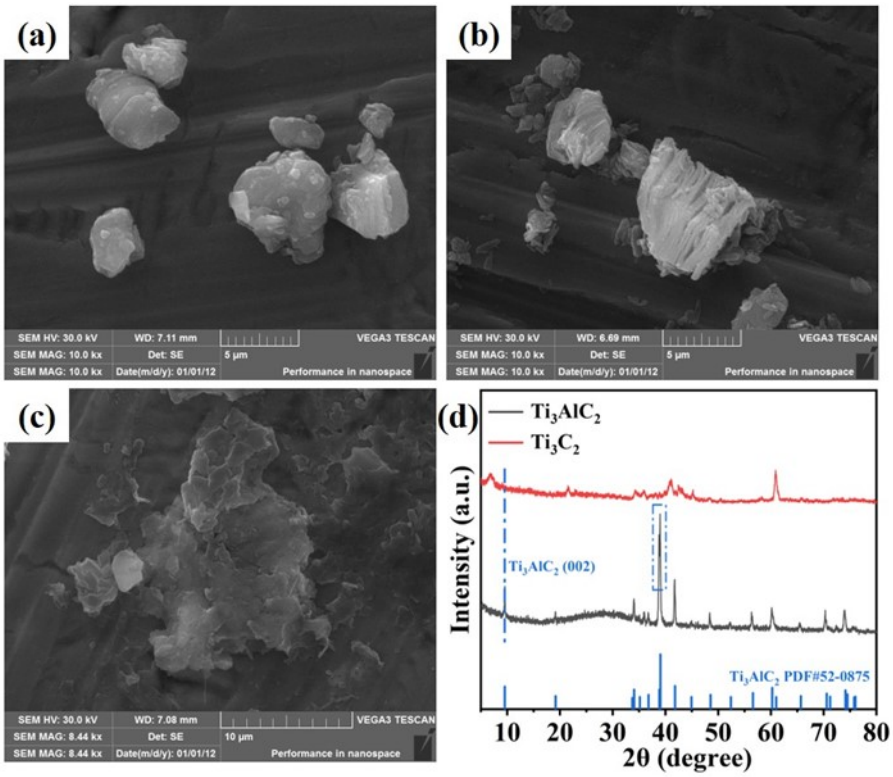

Fig. S3 SEM images of (a) Ti_3AlC_2, (b) multi-layer Ti_3C_2 and (c) single-layer Ti_3C_2 nanosheets; (d) XRD spectra of Ti_3AlC_2 and multi-layer Ti_3C_2 MXene.

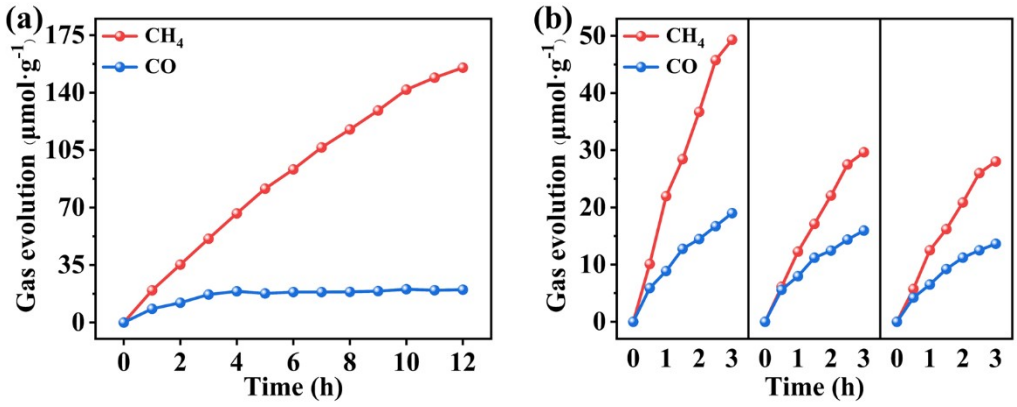

Fig. S4 (a) Long-term stability test plot of photocatalytic CO_2 reduction evolution for 2N-TTC; (b) Cycling stability test plot of photocatalytic CO_2 reduction evolution for 2N-TTC

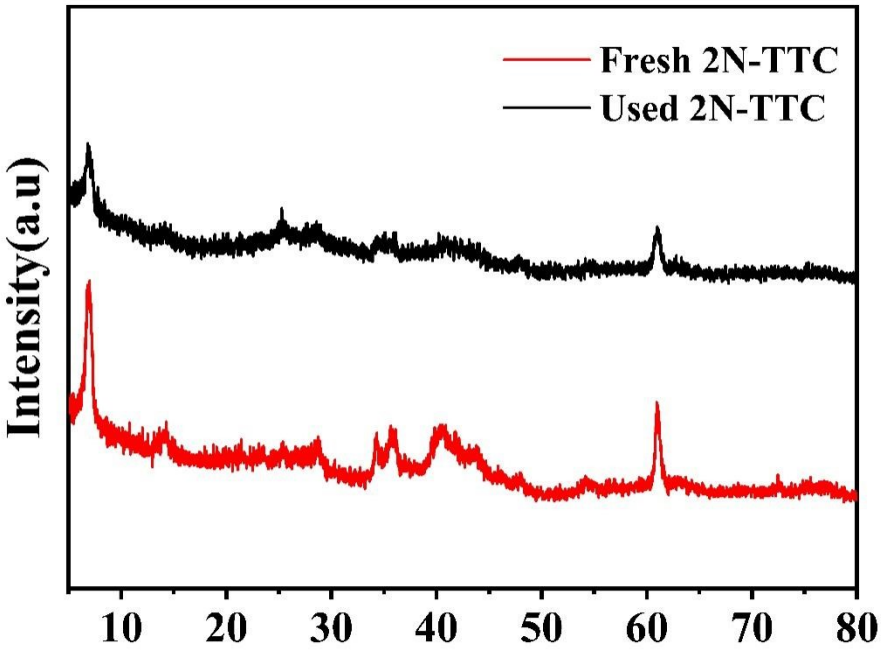

Fig. S5 XRD patterns of 2N-TTC before and after the light reaction

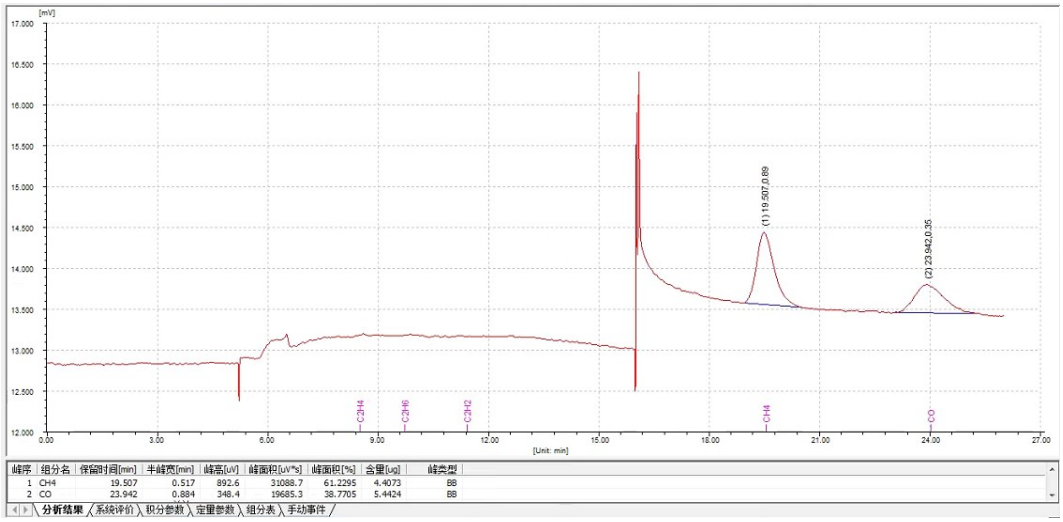

峰序	组分名	保留时间[min]	半峰宽[min]	峰高[uV]	峰面积[uV*s]	峰面积[%]	含量[ug]	峰类型
1	CH4	19.507	0.517	892.6	31088.7	61.2295	4.4073	BB
2	CO	23.942	0.884	348.4	19685.3	38.7705	5.4424	BB

分析结果 | 系统评价 | 积分参数 | 定量参数 | 组分表 | 手动事件

Fig. S6 The chromatogram obtained by the FID detector of the GC9790II chromatography system

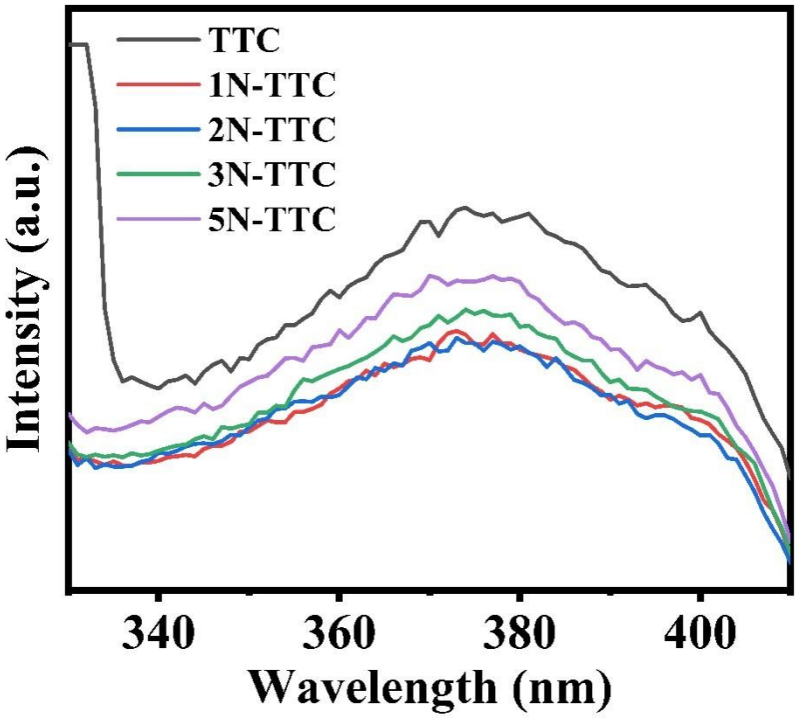

Fig. S7 PL spectra of TTC and N-doped TTC

Table S1 Comparison of the photoreduction activity of structurally related materials

Photocatalysts	Reaction conditions	Products	Yield ($\mu mol \cdot g^{-1} \cdot h^{-1}$)	Selectivity	Ref.
NiAl-LDH@TiO_2/Ti_3C_2-30	Gas-Solid H_2O, CO_2	CO	86.52	99%	[1]
Co-CuS_{1-x}/Ti_3C_2/TiO_2	Gas-Solid H_2O, CO_2	CO	30.8	87.9%	[2]
Pt-TiO_2NW/Ti_3C_2	Gas-Solid H_2O, CO_2	CH4	3.61	79.2%	[3]
$ZnIn_2S_4$/TiO_2/Ti_3C_2	Gas-Solid H_2O, CO_2	CO	7.48	91.2%	[4]
0D–2D NT@ZIS	Gas-Solid H_2O, CO_2	CO	76.2	92.9%	[5]
TiO_2/Ti_3C_2/Cu	Gas-Solid H_2O, CO_2	CH4	12.5	97.7%	[6]
Ti_3C_2-TiO_2-2	Gas-Solid-Liquid H_2O, TEOA, MECN, CO_2	CO	7.8	-	[7]
Au NP/ TiO_2/Ti_3C_2	Gas-Solid H_2O, CO_2	CH4	14.0	86.0%	[8]
2N- TiO_2-Ti_3C_2	Gas-Solid H_2O, CO_2	CH4	17.1	92.3%	This work

References

[1] Lee D E, Devthade V, Abraham B M, et al. An S-scheme heterointerface-engineered high-performance ternary NiAl-LDH@TiO_2/Ti_3C_2 MXene photocatalytic system for solar-powered CO_2 reduction to produce energy-rich fuels[J]. Chemical Engineering Journal, 2024, 480: 148227.

[2] Shao S, Yang F, Kan Z, et al. Two-dimensional QDs-Co-CuS_{1-x}/Ti_3C_2/TiO_2 heterojunction with synergistic unsaturated bimetal sites and sulfur vacancies for highly selective photocatalytic CO_2 reduction[J]. Journal of Colloid and Interface Science, 2025, 682: 104-114.

[3] Charyulu Devarayapalli K, Prabhakar Vattikuti S V, Kim D J, et al. Platinum quantum dots-decorated MXene-derived titanium dioxide nanowire/Ti_3C_2 heterostructure for use in solar-driven gas-phase carbon dioxide reduction to yield value-added fuels[J]. Journal of Energy Chemistry, 2023, 82: 627-637.

[4] Devarayapalli K C, Kim B, Manchuri A R, et al. 2D ultrathin $ZnIn_2S_4$ nanosheets anchored on octahedral TiO_2/Ti_3C_2 Z-scheme heterostructure for enhanced photocatalytic CO_2 reduction[J]. Applied Surface Science, 2023, 636: 157865.

[5] Xu H, Wei Y, Hao S, et al. Mechanistic insight into N-doping-enhanced CO_2 adsorption, activation and selectivity regulation in 0D2D NT@ZIS S-scheme heterostructures[J]. Chemical Engineering Journal, 2026, 527: 171640.

[6] Xu W, Peng Y, Hu D, et al. Molten Salt Synthesis of Ti_3C_2/Cu Cocatalyst for Enhanced TiO_2 Photocatalytic CO_2 Reduction[J]. ChemCatChem, 2024, 16(20): e202400873.

[7] Asghar Z, Rehman Z U, Butt F K, et al. Structural engineering of Ti_3C_2-TiO_2 nanoflowers modified with oxygen vacancy for photocatalytic applications[J]. Renewable Energy, 2025, 248: 123134.

[8] Li Y, Yang Y L, Chen G, et al. Au cluster anchored on TiO_2/Ti_3C_2 hybrid composites for efficient photocatalytic CO_2 reduction[J]. Rare Metals, 2022, 41(9): 3045-3059.